Metal oxide-doped activated carbons from bakery waste and coffee grounds for application in supercapacitors

Philipp Konnerth [a,*], Dennis Jung [a], Jan W. Straten [a], Klaus Raffelt [b], Andrea Kruse [a]

[a] University of Hohenheim, Institute of Agricultural Engineering, Department of Conversion Technologies of Biobased Resources, Garbenstr. 9, 70599 Stuttgart, Germany
[b] Karlsruhe Institute of Technology (KIT), Institute of Catalysis Research and Technology (IKFT), Hermann-von-Helmholtz-Platz 1, 76344 Eggenstein-Leopoldshafen, Germany

ARTICLE INFO

ABSTRACT

The functionalization of sustainable carbon materials and their application in energy storage systems attract more and more relevancy. Bakery waste and spent coffee grounds were chosen as abundant organic residues and found to be suitable starting materials for hydrothermal carbonization and a subsequent chemical activation obtaining carbon contents of > 88%. In situ doping of the hydrochars during carbonization has proven to be a successful method for insertion of Fe_2O_3-, Fe_3O_4- and MnO_2-Nanoparticles into the carbon matrix, supported by XRD analysis and SEM images. Chemical activation with K_2CO_3 led to iron contents up to 18% of iron and around 8% of manganese, respectively, in the corresponding activated carbon. Electrochemical characterization revealed overall higher specific capacitance for activated carbons derived from spent coffee grounds, with a highest of $87F^*g^{-1}$. In contrast, the highest specific capacitance measured for activated carbons originated from bakery waste was $40,3F^*g^{-1}$.

1. Introduction

In the last decades, numerous of new energy storage systems drew great attention, due to rising energy demands of global population. Electrical double layer capacitors (EDLCs) and Lithium-Ion-Batteries (LIBs) are the promising electrochemical systems for future applications in electromobility, portable electronic systems and storing of excess energy in power grids [1]. They are able to store charges quickly and efficiently, thus helping to generate renewable energy and convert it into a usable form. EDLCs especially, are electrochemical systems to provide energy in a fast and reliable manner due to high capacitance and cycling numbers as well as fast charging and discharging mechanisms based on electrostatic interactions, specific adsorption and reversible electron transfers [2,3]. To remain these characteristics, the faultless operation of the system has to ensure and depends significantly on the electrode material. Because of its chemical stability, high adsorption properties and high specific area, activated carbon (AC) became a suitable material considering EDLC electrodes. Recently, efforts have been made to obtain low-cost carbon-based materials for convenient and practical application in electrochemical devices [1,4–6]. In this case, biomass became an attractive precursor for carbon electrodes besides conventional materials such as ceramic, polymers and metal oxides [6]. An interesting field of research is the suitability of agricultural residues as an abundant and renewable resource for EDLC electrode materials. The application of technical processes enable the conversion of the starting materials into highly porous carbon products. In those terms, thermochemical syntheses as hydrothermal carbonization (HTC) and pyrolysis/chemical activation are beneficial for functionalization of organic matter like biomass and agricultural residues. HTC takes place in a closed system within a temperature range between 170 and 350 °C [7]. Throughout this process, the initial carbon matrix of the biobased starting materials underlie numerous of parallel and consecutive reactions such as dehydration, decarboxylation, polymerization and aromatization [8]. Yet, the kinetics of these cascades of reactions are not fully understood. However, the hydrothermal decomposition of biopolymers of the biomass leads to restructuring of the carbon matrix on a molecular basis and building of an aromatic carbon network with abundant functional groups, called hydrochar (HC) [9]. Also, the modification of these char-like products with nanoparticles can have an

* Corresponding author.
E-mail address: philipp.konnerth@uni-hohenheim.de (P. Konnerth).

Production and hosting by Elsevier

influence in the carbon material properties. Carbon materials can promote the formation of core–shell nanostructures by encapsulating metal oxides (e.g. SnO_2, Fe_2O_3, Fe_3O_4) present during hydrothermal carbonization [10,11]. A following pyrolysis or activation treatment at high temperatures between 500 and 900 °C provide better adherence to the carbon matrix [12]. Moreover, activation leads into formation of highly porous carbon with high surface areas and enhanced adsorption properties that are crucial for the characteristics of EDLC-electrodes.

In the last decade, several studies reported on the preparation of functionalized carbon materials and EDLC electrodes derived from banana fibers, cashmere, coconut shells, coffee grounds, starch and corncob while applying these methods [4–6,12–14]. However, carbonaceous materials are still facing drawbacks regarding their utilization as electrodes for supercapacitors. For instance, ACs can suffer from poor permittivity and polarization ability as well as low electrical conductivity due to its amorph character [15,16]. Redox-active species like Fe_2O_3, Fe_3O_4, MnO_2, NiO and RuO_2 influence the energy storage mechanisms occurring at the electrode surface [17–19]. These so called pseudocapacitors enable charge transfers (faradaic currents) due to reversible redox reactions between the electrode and the electrolyte species. In contrast, EDLCs only provide double layer capacitance due to electron transfers of the adsorbed charge carriers [5,20]. Thus, it has been reported that heteroatom doping and insertion of MO nanoparticles can improve the electrochemical performance of the device due to the reversible charge storage [18,20].

In this study, we examine the physicochemical properties and electrochemical performance of biobased electrode materials, as well as the carbon and mass balance, which serve as a basis for life cycle assessment. The latter, because a good sustainability of the process could only be reached if no or not much carbon is lost, during conversion. Therefore, the two organic residual biomasses, bakery waste (BW) and spent coffee grounds (SCG) have been chosen as precursors. HTC pretreatment with in situ doping of Fe_2O_3-, Fe_3O_4- and MnO_2-nanoparticles and a subsequent activation process were carried out to obtain activated carbon containing metal oxides. The influence of the selected biomasses and metal oxide nanoparticles on thermochemical processes and electrochemistry were evaluated. The production of "green" electrode materials represents a future-orientated and sustainable route within a bioeconomy concept.

2. Materials and methods

2.1. Materials

Spent coffee grounds (SCG) and bakery waste (BW) were obtained from the cafeteria of the University of Hohenheim, Stuttgart, Germany and from bakery Schultheiss in Ostfildern-Nellingen, Germany.

Metal oxide nanoparticles Fe_2O_3 (20 – 40 nm), Fe_3O_4 (50 – 100 nm), MnO_2 (99.996%) and carbon black (>99,9%) were purchased from Alfa Aesar (by ThermoFischer Scientific), Kandel, Germany. Potassium carbonate anhydrous (K_2CO_3) was obtained from VWR Chemicals, Solon Ohio, USA. Polytetrafluoroethylene (PTFE) and Sulfuric Acid (Suprapur, 96%) was provided by Sigma Aldrich (Merck KGaA), Darmstadt, Germany. Norit SAE Super and Norit SXRO Plus activated carbon were purchased from Cabot, Netherlands. All commercially obtained chemicals were used as received without further purification.

2.2. Instrumentation

An air-fluxed STA Jupiter 449 F5 thermogravimetric analyzer (Netzsch, Gemany) and a Euro EA CHNS-analyzer (HEKAtech, Germany) were used for TGA and determination of the elemental composition of the samples. The oxygen content of the elemental sample composition was calculated by difference.

Heavy metal analyzes were performed with a 5110 ICP-OES and an ICP-OES 725-ES system (Agilent, Germany) after sample treatment in a multiwave 3000 microwave digester (Anton Paar, Germany). Field-emission scanning electron microscopy (FESEM, referred to as SEM in this article) was performed with a DSM 982 Gemini (Carl Zeiss Ltd., Germany). X-ray diffraction (XRD) measurement was performed using a AXS D8 Advance diffractometer (Bruker, Germany) with CuKα radiation.

Surface and bulk characterization has been subjected using an Alpha II Platinum-ATR unit (BRUKER, Germany) and a BRUKER Avance Neo 400 Wide bore spectrometer operating at 9,4 T (^1H frequency 400,182 MHz, ^{13}C frequency 100,629 MHz). Electrochemical characterization was carried out using a computer controlled Autolab PGSTAT101 potentiostat (Metrohm, Germany).

2.3. Experimental

2.3.1. Synthesis of hydrochars and activated carbons

SCG and BW were dried over night at 105 °C and used as starting materials. Pure hydrochars (HC) were obtained by mixing 150 g of deionized water and 25 g of dry biomass and sealing in a 250 ml stainless steel autoclave. HTC was carried out at a reaction temperature of 220 °C for 2 h. Throughout carbonization, the pressure inside the autoclave reached between 36 and 42 bar. Metal oxide-doped hydrochars were synthesized by adding 4.76 wt% of Fe_2O_3, Fe_3O_4 or MnO_2 nano powder to the dispersion. After synthesis, the HCs were filtrated and washed with 1000 ml of deionized water as well as dried overnight at 105 °C.

Pure and metal oxide-doped HCs were activated in a stainless steel pyrolysis reactor with nitrogen flux of 20 L*min^{-1}. K_2CO_3 was utilized as an activation agent. A mass ratio of 2:1 (weight of K_2CO_3 : weight of hydrochar) material was chosen for the activation process. A muffle furnace was preheated until inside temperature reached 800 °C. After placing the reactor inside the furnace, reaction time was set to 2 h, starting as soon as the inside temperature reached again 800 °C. After activation, ACs cooled down to room temperature and had been filtrated and washed with 1 L of deionized and 2 L of boiling deionized water. Finally, the ACs were dried overnight at 105 °C.

Yields of hydrochars and activated carbons were calculated as follow:

$$Y = \frac{m(HCorAC)}{m(SM)} * 100 \tag{1}$$

While m(HC or AC) refers to the mass of hydrochars and activated carbons respectively. The mass m(SM) is considered to be the mass of the starting material used for thermochemical conversion. HC and AC synthesis were replicated once.

Carbon Yield was calculated using equation (2):

$$C_{yield} = Y * \frac{C_X}{C_B} \tag{2}$$

Y is the yield that was calculated using Equation (1). C_B is the carbon content of biomass in wt.-% and C_x refers to the carbon content of HC and AC, respectively, in wt.%.

2.3.2. Physical chemical characteriziation

The ash content of the HC samples was determined in a muffle furnace at 815 °C for 2 h, following the standard DIN 51719. Ash content of AC samples were analyzed via thermogravimetric analysis setting a heating rate of 10 K*min^{-1} until the temperature of 815 °C was reached.

ICP Analysis was performed to determine the inorganic compounds of the samples. Therefore, untreated biomass as well as undoped and MO-doped HCs and ACs were treated by microwave-assisted digestion in a 37% HCl- and 65% HNO$_3$-mixture (volume ratio 1:5) prior to analyzed. The quantification of elements in AC-SCG-Fe$_3$O$_4$ were conducted after solving the samples in a mixture of aqua regia and hydrofluoric acid supported by microwave digestion. Wavelength selection and method development followed DIN EN ISO 11885.

2.3.3. Surface and bulk characterization

IR-spectroscopy has been subjected to determine functional surface groups of HC and AC. Absorption of functional groups within the wavelength range of 400 – 4000 cm^{-1}. The ^{13}C solid-state NMR spectra were acquired by filling and pressing the dried and ground samples manually in a 4 mm ZrO$_2$ rotor with a Kel-F cap. Rotational frequence was set to 10 kHz during the measurement. The chemical shift is referred to adamantan (29,45 ppm and 38,48 ppm, respectively), which was measured in a separate experiment just before. Cross polarization was applied to increase the ^{13}C intensity). Spectra were acquired with spectral width 50.000 Hz, time domain 1800, pulse with 3,5 μs and relaxation delay 5 s. 15,000 scans were accumulated to lower the signal to noise and the FID was multiplied with a window function of 20 HZ before fourier transformation.

2.3.4. Electrical conductivity

Electrical Conductivity of ACs was examined by adapting the method described by Hoffmann et. al [21]. Therefore, an acrylic glass cylinder, fixed on a brass base, was filled with sample material (ACs). The upper part consisted of a brass stamp with the same diameter of the glass cylinder to ensure good contact between the stamp and the sample. Electrical conductivity was measured and calculated as followed: First, the upper part was weighed down by using 2, 5 and 10 kg weights as ballast. After, the resistance was measured in dependence of the compressibility and decrease in height respectively, of the sample inside acrylic glass column. Finally, the electrical conductvity was calculated using equation (3):

$$\kappa = \frac{h}{R * A} \tag{3}$$

where κ is the electrical conductivity (Ω / m), h the decrease in height (cm), R the electrical resistance (Ω) and A the stamp area (cm^2).

2.3.5. Electrochemical characterization

Electrochemical Analysis was carried out in a three electrode system. Working electrodes have been prepared as follows: Fabricated ACs and carbon black were mixed in a wt.-ratio of 2:1 (50 mg : 25 mg). Furthermore, the solid mixture was dispersed in 1.5 ml of ethanol and 10 μL of PTFE, used as a binder, was added. The dispersion was stirred for 1 h at 500 rpm. Finally, 70 μL of the mixture was transferred on a carbon black coated aluminum carrier foil (Al@CB foil) and dried overnight at room temperature. For reference purposes, two commercial activated carbons (I-AC), SAE Super and SXRO Plus, were also used for electrode fabrication after the procedure described above.

The electrochemical characterization was conducted using a three electrode assembly. The aforementioned electrodes were applied as working electrodes (WE). A Pt sheet electrode (Metrohm, Germany) and reversible hydrogen electrode (RHE) was used as counter (CE) and reference electrode (RE), respectively. 0,5 M H$_2$SO$_4$ solution was utilized as electrolyte. Before measuring cyclic voltammetry (CV), the cell was degassed with nitrogen for 5 min. CV was performed between a potential range of −0,2 –

1,2 V under variation of the scan rates (100 mV*s^{-1} and 5 mV*s^{-1}). Specific capacitance was calculated as followed:

$$C = \frac{\int_{v1}^{v2} I(v)dv}{m * r * \Delta V} \tag{4}$$

whereby the numerator represents the integral of the current I as a function depending on the potential v between the potential limits $v1$ and $v2$. Denominator consists of the product of m as the mass of active material, r as the scan rate and ΔV as the potential interval.

3. Results

Table 1 displays the solid yields of HCs and ACs with respect to the starting materials. Yields of HCs are generally 2 – 7,6 times higher than those of the ACs. Highest yields can be observed for Fe$_2$O$_3$- and Fe$_3$O$_4$-doped hydrochars and are around 3 – 4% higher than the undoped reference samples. However, HCs from BW exhibit lower yields than chars derived from SCG. In contrast, iron-doped ACs show lowest solid yields within all AC samples and are around 6% and 6 – 8% lower than undoped ACs of BW and SCG respectively. Also, MnO$_2$-doped ACs from BW show slightly lower solid yields unlike ACs from SCG, where higher yields can be observed.

The elemental composition and ash contents of the starting materials BW, SCG such as undoped and doped HCs and ACs also listed in table 1, clearly indicate an increase of the carbon contents. A simultaneous decrease in oxygen contents can be observed within all HCs in relation to the starting materials. It can be observed, that the increase of carbon in HCs of BW after HTC is higher than for SCG. Furthermore, a slight decrease of the ash content of undoped HCs can be noticed while the ash content for metal oxide-doped (MO-doped) HCs rises significantly. Results of ICP-Analysis of in situ doped HC-BW and HC-SCG indicates uptake of MO-Nanoparticles as high amounts of iron and manganese can be detected.

After chemical activation, a carbon content of 86 – 88% can be obtained for pristine SCG-ACs and BW-ACs, respectively. Also, for MO-doped carbons, a high proportion of ash can be noted. For Fe$_3$O$_4$-doped ACs from SCG, iron contents constitute almost 20% of the sample weight. Manganese contents of MnO$_2$-doped ACs reach up to 8 wt-%.

As represented in the Van-Krevelen-Diagram (Fig. 1), a drastic decrease of H/C- and O/C-ratios along the dehydration and decarboxylation curves can be observed during carbonization. Yet, HC-SCGs obtain a higher H/C ratio whereas the O/C ratio is approximately similar to that of HC-BW samples.

Fig. 2 depicts SEM images of pristine and MO-doped HCs derived from SCG. The highlighted areas show microstructures formed during HTC (blue), ion oxide (yellow) and MnO$_2$ (red) particles. The hydrochars exhibit an amorphous and porous surface structure. MO-doped samples show the superficially adherent metal oxide species. MnO$_2$ nanoparticles especially tend to form large clusters on the char surface. Additionally, the XRD pattern of the respective Fe$_2$O$_3$-doped hydrochar sample is shown in Fig. 2D. Interestingly, Fe$_2$O$_3$ is no longer in its primary oxidation state, as the nanoparticles seem to be reduced to Fe$_3$O$_4$ under hydrothermal conditions.

ATR-IR-Spectroscopy of HCs and ACs are illustrated in Fig. 3.

For HCs from BW (Fig. 3A), a noticeable reduction of the absorption bands at 807 – 1183 cm^{-1}, 2826 – 2979 cm^{-1} and approximately 3000 – 3620 cm^{-1} can be seen. Those signals are assigned to O–H bending and C–O stretching as well as C–H- and O–H-stretching of aliphatic compounds, hydroxyl and ester/ether groups. The peaks at 1560 cm^{-1} and 1690 cm^{-1} respectively, originate from C = O and C = C vibrations of aromatic rings. The double

Table 1

Yields and elemental composition of starting materials, hydrochars and activated carbons.

Sample	Yield (%)[a]	Yield (%)[b]	C-Yield (%)[c]	C (%)	H (%)	S (%)	O (%)	N (%)	Fe (%)[b]	Mn (%)[b]	Ash (%)
BW (pure)	–	–	–	44,6	6,5	0,1	45,7	2,4	< 0,01	< 0,01	0,7
HC-BW	45,2	–	71,0	69,7	5,0	0,1	21,3	3,4	< 0,01	< 0,01	0,4
AC-BW	20,0	44,2	39,6	88,4	0,3	–	n.m.*	0,8	< 0,01	< 0,01	n.m.
HC-BW-Fe$_2$O$_3$	48,4	–	75,3	62,7	4,6	0,1	19,9	3,0	4,85	< 0,01	9,6
AC-BW-Fe$_2$O$_3$	13,8	28,5	20,5	65,9	0,3	–	n.m.	0,6	n.m.	n.m.	n.m.
HC-BW-Fe$_3$O$_4$	49,2	–	77,4	63,2	4,6	0,2	19,0	3,0	n.m.	n.m.	9,8
AC-BW-Fe$_3$O$_4$	14,4	29,3	22,8	71,1	0,3	–	n.m.	0,6	n.m.	n.m.	n.m.
HC-BW-MnO$_2$	41,0	–	62,9	63,2	5,0	0,1	21,4	3,0	n.m.	n.m.	6,7
AC-BW-MnO$_2$	18,3	44,8	34,2	83,1	0,4	–	n.m.	1,0	< 0,01	8,58	n.m.
SCG (pure)	–	–	–	53,3	7,2	0,1	36,2	2,8	< 0,01	< 0,01	0,7
HC-SCG	56,6	–	73,3	68,8	7,2	0,1	20,8	2,5	< 0,01	< 0,01	0,3
AC-SCG	15,8	28	25,6	86,4	0,4	–	n.m.	1,1	< 0,01	< 0,01	n.m.
HC-SCG-Fe$_2$O$_3$	60,9	–	78,8	63,2	6,6	0,1	19,2	2,5	3,57	< 0,01	8,3
AC-SCG-Fe$_2$O$_3$	7,9	13	8,3	56,0	0,3	–	0,5	0,4	n.m.	n.m.	43,2
HC-SCG-Fe$_3$O$_4$	59,4	–	77,9	64,8	6,6	0,1	18,6	2,6	n.m.	n.m.	7,3
AC-SCG-Fe$_3$O$_4$	9,8	16,7	12,2	66,6	0,3	–	4,3	0,5	18,6	< 0,01	27,1
HC-SCG-MnO$_2$	56,3	–	72,9	64,9	7,0	0,1	19,5	2,6	n.m.	n.m.	5,9
AC-SCG-MnO$_2$	17,8	31,6	26,7	79,1	0,3	–	9,0	0,4	< 0,01	7,56	11,2

* n.m.: not measured.
[a] Mass yield related to biomass.
[b] Mass yield related to hydrochar.
[c] Carbon yield related to biomass.
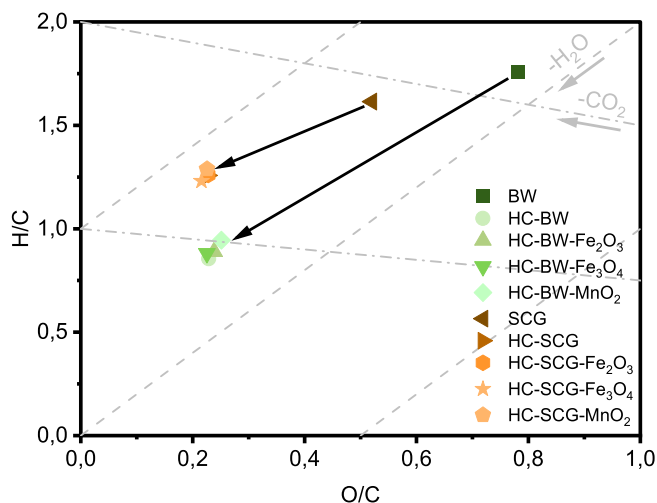
Fig. 1. Van-Krevelen-Diagram of pure Biomasses and the corresponding Hydrochars (H/C and O/C are molar ratios).

peak at 2294 – 2392 cm^{-1} can be ascribed to C = O vibration of atmospheric CO_2 trapped inside the pore structure.

IR spectra of HCs from SCG in Fig. 3B show similar bands to those of the starting material. A decrease of the broad band between 833 and 1207 cm^{-1} corresponding to the C–O stretch of ester or ether and hydroxy groups can be noticed. For the sharp peak at 2774 – 2983 cm^{-1} linked to C–H stretch aliphatic compounds, no change in intensity can be observed. Further on, the bump-like absorption band from 3028 to 3615 cm^{-1} assigned to hydroxy groups is slightly reduced. Iron-doped HCs show additional bands in the wavenumber range of approximately 490 – 662 cm^{-1}.

IR spectra of the ACs, illustrated in Fig. 3C and D, show similar absorption bands irrespective of the starting material. Weakened and broadened bands in a wavenumber range of 900 – 1300 cm^{-1} can be observed in all spectra. A significant band between 1580 and 1640 cm^{-1} is ascribed to C = C vibration of aromatics.

For a more detailed insight of the chemical composition, regarding the formation of the carbon matrix of pure SCGs and HTC-treated SCG, ^{13}C Nuclear Magnetic Resonance Spectroscopy (^{13}C NMR- Spectroscopy) was performed.

The ^{13}C NMR spectrum of pure SCG (Fig. 4A) shows low intensity between 20 and 50 ppm assigned to sp^3-carbons of aliphatic compounds (CH, CH$_2$ and CH$_3$), followed by various superimposed signals between 50 and 95 ppm with a highest intensity at approximately 72 ppm. These include cellulose signals and C–O bonds of the pristine carbon structure. Higher chemical shifts at 100 – 160 ppm are assigned to C = C double bonds (isolated, conjugated and aromatic), but show only low intensity in the SCG spectrum. At the left end of the spectrum (approx. 167 – 185 ppm), another noticeably signal can be detected originating from carboxylic groups.

For the ^{13}C NMR spectrum of HC-SCG in Fig. 4B, the chemical shifts between 20 and 50 ppm become much more evident. Simultaneously, the signals from 50 to 95 ppm and 167–185 ppm are decreasing. The signal at 110 ppm is slightly changed in the hydrochar product and a broad new resonance between 110 and 165 ppm is observed. Without further and more sophisticated experiments the assignment of the resonances between 100 and 160 ppm must remain very general as "C = C double bonds and aromatics", which can include also phenolic or furanic species. Though the intensity is not high, a significant resonance at 210 ppm has developed, which can be assigned to ketones.

MnO_2-doped hydrochars from SCG (Fig. 4C) show generally the same chemical shifts as undoped hydrochars, but with a higher contribution of alkyl signals, a lower resonance of double bonds and aromatics and no intensity in the region of ketones.

Fig. 5 show the electrical conductivity (EC) of all ACs with respect to the applied pressure. For all carbons, an increase of the electrical conductivity can be observed as the applied pressure rises. Carbon black was chosen as reference material with highest conductivity at maximum pressure.

ACs from SCG reveal higher electrical conductivities than the BW references. For BW-ACs, all MO-doped ACs show lower conductivity values with increasing pressure than undoped carbons. For SCG-ACs, a different trend can be observed. Although, MnO_2-doped carbons show the lowest electrical conductivities as well, iron-doped ACs obtained higher conductivity than undoped carbons values as pressure increases.

Fig. 6 depicts the cyclic voltammetry (CV) of undoped/pristine and MO-doped ACs under variation of the scan rate.
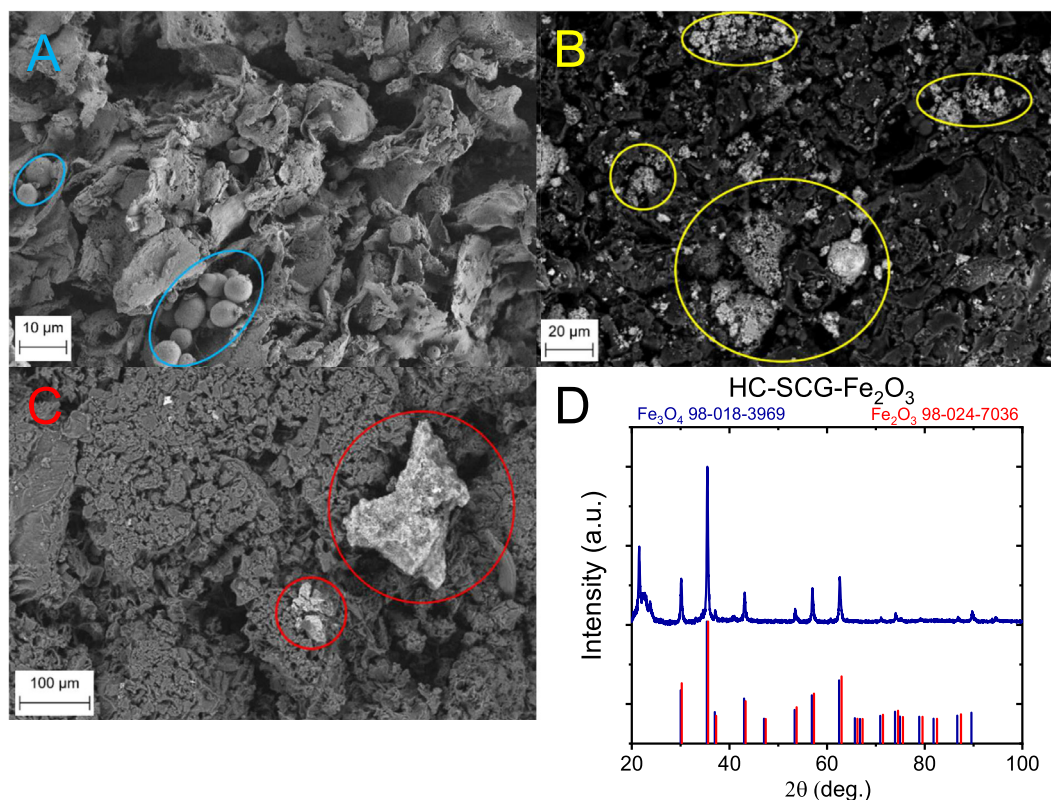
Fig. 2. SEM images of pristine HC-SCG (A), Fe_2O_3-doped HC-SCG (B) and MnO_2-doped HC-SCG (C). D displays the XRD pattern of Fe_2O_3-doped HC-SCG.

Lower scan rates result in a higher specific capacitance for all ACs. CV curves show two different shapes during electrochemical cycles at 5 mV*s^{-1}. First of all, characteristic anodic and cathodic half-cycles within the potential range and secondly, a less pronounced and diminished cathodic half-cycle at lower potentials.

The specific capacitance represented in Fig. 7A and B show high deviations for ACs originating from SCG. The overall highest capacitance of 87F*g^{-1} can be observed for AC-SCG-MnO_2 at a scan rate of 5 mV*s^{-1}. The highest obtained specific capacitance for ACs derived from BW is around 40.3F*g^{-1} containing Fe_2O_3-doping. However, the standard deviation of specific capacitance is high since the corresponding replicates of the electrodes only measured specific capacitance of 11.4F*g^{-1} and 14.7 F*g^{-1}, respectively, at the same scan rate. Lowest measured specific capacitance can be observed for AC-BW-MnO_2 with 0.3F*g^{-1} at a scan rate of 0.1 V*s^{-1} and 7.7 F*g^{-1} at a scan rate of 5 mV*s^{-1}, respectively.

4. Discussion

4.1. Physical chemical characterization

The formation of carbonaceous solid products derived from hydrothermal carbonization crucially depends on the chemical composition of the starting material. As for biomasses, with high fractions of compounds of low thermal stabilities, complex reaction pathways can be observed throughout hydrothermal treatment. The degradation of starch starts at temperatures > 180 °C due to hydrolysis of α-1,6-glycosidic bonds of glucose within the biopolymer [8]. Further, the isomerization to fructose and consecutive dehydration to 5-Hydroxymethylfurfural, followed by polymerization of the furfural, leads to formation of the hydrochar [22]. These conversion reactions are accompanied by a significant release of volatiles, mainly H_2O and CO_2, and the transfer of organic compounds to the liquid phase. Hence, HCs from BW generally

obtain lower yields compared to SCG due to strong thermal degradation. In contrast, SCG contains of both, thermolabile and thermally stable compounds under hydrothermal conditions. Alongside with cellulose, SCG also consist of caffeine, lipids and to a smaller extents lignin [23]. The latter mentioned components have a generally higher thermal stability, are not subjected to decomposition and also remain in the HCs. This results into higher yields compared to chars from BW. Besides, previous torrefaction and subsequent brewing of coffee beans already leads to a decrease of volatiles and washing out of soluble compounds as fructose, galactose and arabinose etc. [23]. Therefore, smaller amounts of decomposable and hydrolysable components are available to participate in the reaction pathways. This also contributes to the superior solid yields listed in table 1.

Fig. 1 (Van-Krevelen-Diagram) gives a better understanding of the ongoing reactions and the role of the precursor material in hydrothermal processes. A high decrease of the carbon and oxygen contents is ascribed to decarboxylation reactions occurring during the hydrothermal process [24]. Additionally, reduced hydrogen contents are assigned to dehydration reactions [8,24]. Due to the conversion mechanisms of BW during hydrothermal pretreatment, the changes in H/C- and O/C-ratios are more drastic than with SCG. As mentioned before, the previous heat treatment (torrefaction) of coffee beans is crucial for the further release of volatiles during HTC. A slighter decrease of the ratios can be assigned to this. In fact, SCG remains more stable under hydrothermal conditions as it can be hydrolyzed only to a certain extend. Therefore, a solid-to-solid-conversion pathway is more likely in context of hydrothermal carbonization of SCGs.

Generally, the ash contents decrease after hydrothermal treatment due to partial transfer of inorganic compounds as potassium-, manganese compounds etc. into the liquid phase. An increase of the ash contents can be observed for both, MO-doped HCs and ACs, which is an indicator for successful insertion of
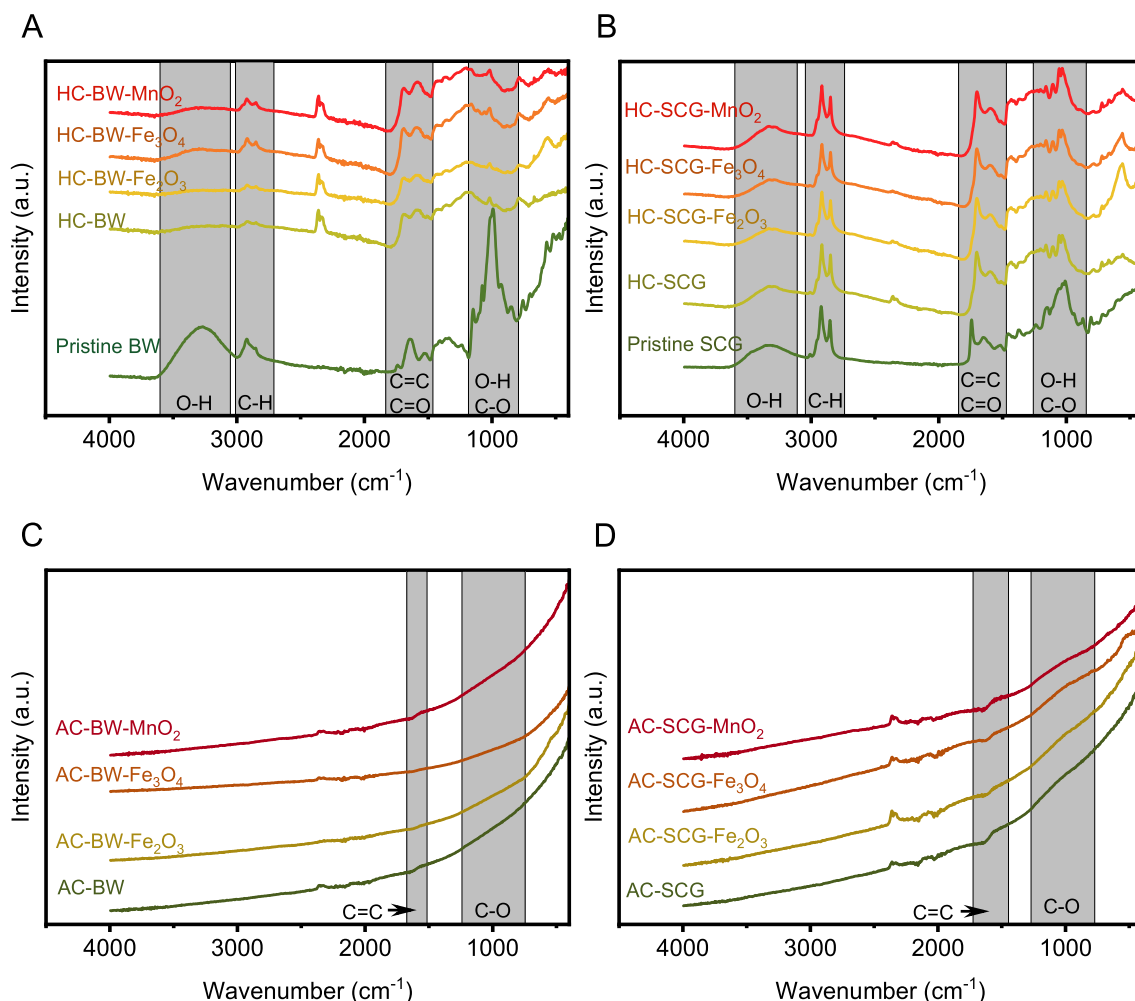
Fig. 3. IR-Spectra of HC-BWs (A), HC-SCGs (B) and the corresponding ACs of unloaded and MO-doped samples (C, D).

MO-nanoparticles into the carbonaceous hydrochar matrix. This is also supported by the results of ICP analysis in table 1. Solid yields of undoped ACs are generally lower with respect to the hydrochars, whereas the carbon fractions increase significantly. Due to thermal treatment of the hydrochars, this leads to a gradual release of volatiles as CO, CO_2 and H_2O results into lower yields and higher relative carbon contents. Chemical activation in presence of K_2CO_3 as an activation agent also catalyzes the evolution of CO during the process [25]. This is also supported by observation of the low carbon yields. The carbon yields of hydrochars, displayed in table 1, are overall higher than the corresponding activated carbon, since more carbon of the starting materials remains in the chars. ACs derived from BW exhibit slightly higher C-yields than the SCG reference, ranging around 39,6% for undoped ACs. That is because of decomposition of the before mentioned hydrothermal stable compounds (e.g. lipids, waxes, caffeine), which are still contained in the hydrochars derived from SCG. Fe_2O_3- and Fe_3O_4-doped ACs show the lowest carbon yields, which can be ascribed to the catalytic release of CO by the nanoparticles as described in the following. In the presence of carbon, iron oxide nanoparticles are reduced in an inert atmosphere at temperatures > 400° C, since carbon will act as a reducing agent [12]. The reduced iron species, especially in the form of elemental iron and iron carbide (Fe_3C), can further catalyze the release of H_2, H_2O and CO [12,26,27]. The observations made on the decreasing solid yields of iron oxide doped ACs indicate possible catalytic release of volatiles along with the reduction

pathways of iron oxide nanoparticles. Unlike, it can be assumed, that MO nanoparticles may have no catalytic effect on the release of volatiles on the hydrochar product under hydrothermal conditions. This is also supported by the Van-Krevelen-Diagram (Fig. 1), since the H/C and O/C atomic ratios of HCs are all in the same range. However, the presence of carbon might lead to a reduction of Fe_2O_3 to Fe_3O_4 during HTC. The SEM images in Fig. 2 reveal that the nanoparticles tend to adsorb and adhere to the char surface in case of HCs derived from SCG. The highlighted areas show the agglomeration and inhomogeneous distribution of the iron and manganese oxide particles on the carbonaceous surface. MnO_2 particles form much larger agglomerates, which remain on the SCG derived HC surface (Fig. 2B). It is assumed that free nanoparticles form micro-scale structures throughout the HTC process, which partly remain as cluster like structures on the char surface. The rest is dispersed in the process water and will be removed by filtration. However, for MO-doped HC-BW samples the nanoparticle distribution remains unclear. In 2006, Xianjin Cui et al. found that Fe_2O_3-nanoparticles were trapped and enclosed by decompositions products of starch during hydrothermal carbonization. TEM-based investigations have demonstrated the sheathing effect of the microspheres of the particles obtained from starch [11]. Therefore, a similar case can be made regarding Fe_2O_3-doped HCs from bakery waste. Interestingly, the XRD pattern of a Fe_2O_3-doped HC (Fig. 2D) hint that the nanoparticles are subjected to reduction reactions during hydrothermal pretreat-
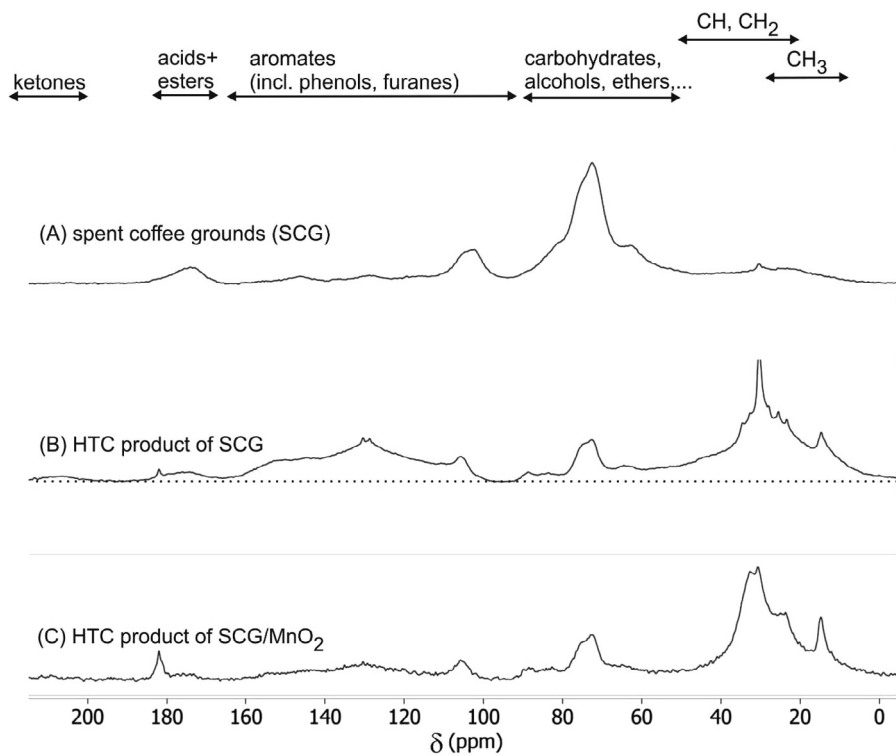
Fig. 4. ^{13}C NMR of untreated SCG (A), undoped (B) and MnO_2-doped Hydrochars (C) from SCG.
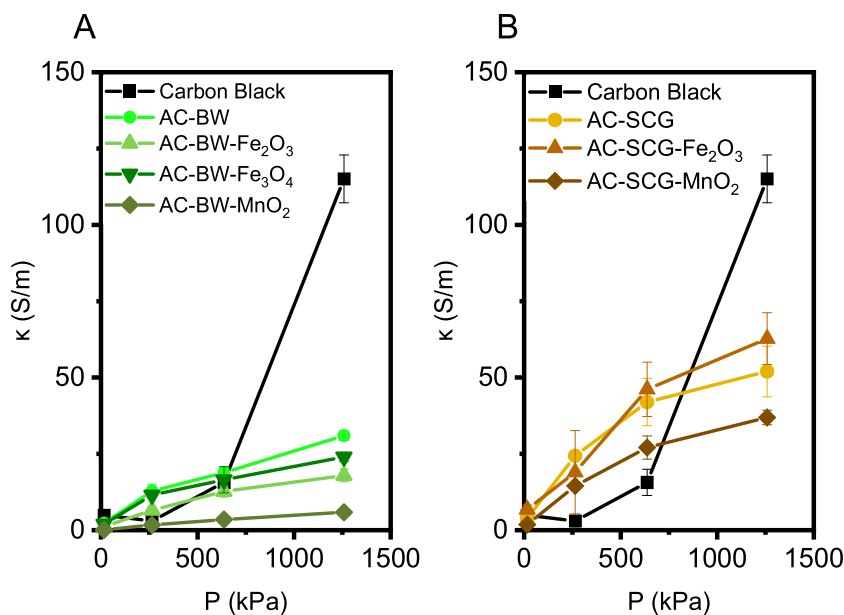

Fig. 5. Electrical conductivity of undoped and MO-doped Activated Carbons derived from BW (A) and SCG (B). Carbon Black (black line/squares) is used as reference material.

ment, thus undergoing a phase transformation to Fe_3O_4. In contrast, the diffractogram of MnO_2-doped HCs exhibited a broad humped peak and was not included in the results of this work. This indicates that MnO_2 is mainly present in a disordered and amorphous state. The reduction of Fe_2O_3 is certainly surprising since the reduction in acidic aqueous media (note that the process water of HTC has a low pH) is usually slower than in basic solutions [28,29]. However, it has been observed that the kinetics of the phase transformation became heavily accelerated during hydrothermal processes when organic compounds with functional

nitrogen groups were added [28]. SCG contains high amounts of proteins and traces of free amino acids, which can serve as possible nitrogen sources [23]. Besides, carbon is known as reducing agent towards iron oxide at high temperatures – albeit predominantly under inert, non-aqueous conditions [12,27]. It can be considered that the chemical species present (e.g. carbon and nitrogen functional groups) may play a crucial role in the reduction pathway of Fe_2O_3 during HTC. However, the reduction of hematite in presence of lignocellulosic residues and their influence has not yet been investigated and has to be studied more closely.
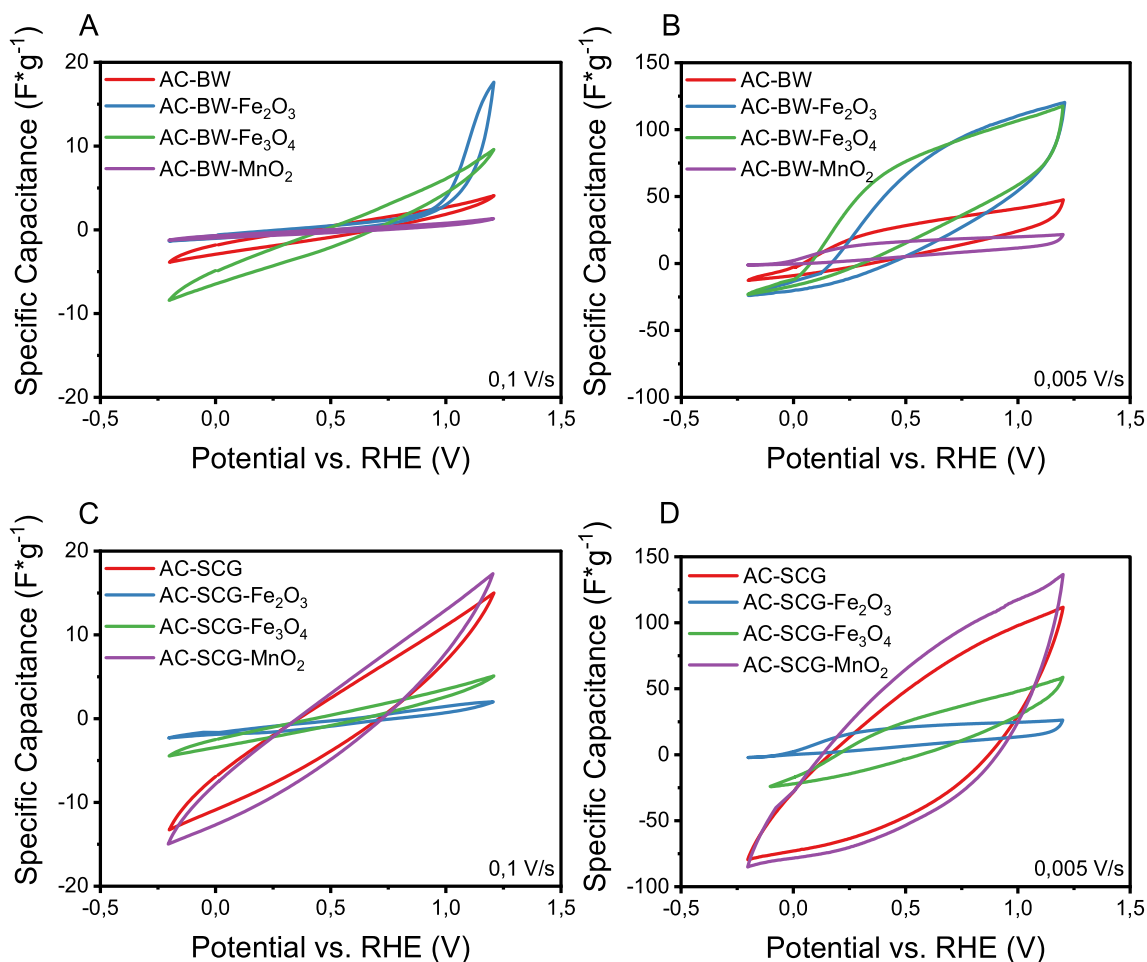
Fig. 6. Cyclic voltammetry of undoped/MO-doped activated carbons derived from BW (A,B) and SCG (C,D) at scan rates of 100 mV*s^{-1} and 5 mV*s^{-1}.
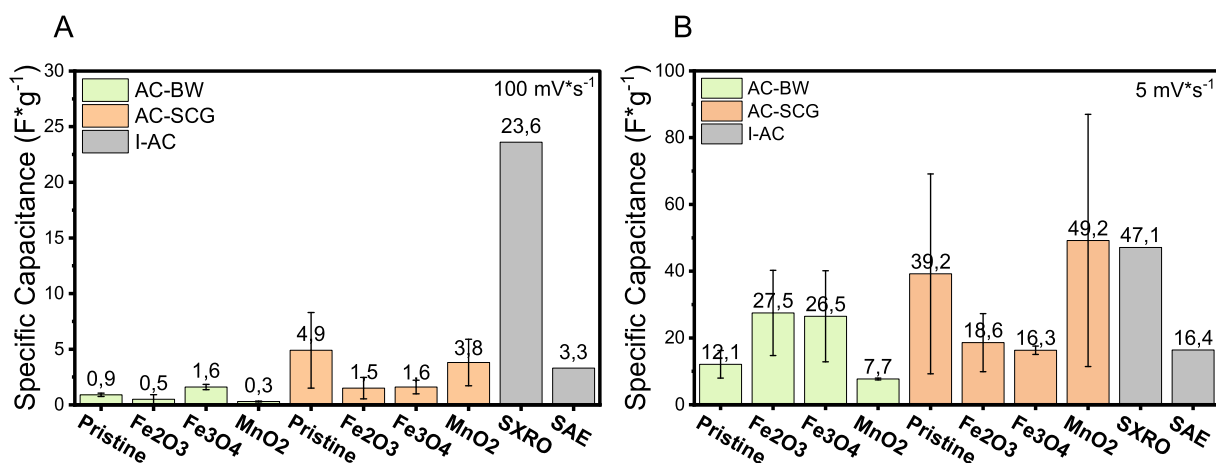

Fig. 7. Specific capacitance of undoped/MO-doped and industrial activated carbons at scan rates of 0.1 V/s (A) and 0.005 V/s (B). I-AC = commercial activated carbons.

4.2. Surface and bulk properties of activated carbons

The consideration of the ATR-IR spectra of hydrochars (Fig. 3A) from bakery waste confirm the statements made before. The decrease of the absorption bands at wave numbers 800 – 1200, 2826 – 2979 and 3000 – 3620 cm^{-1} corresponding to oxygen functional groups (e.g. ether, hydroxyl), aliphatic compounds and hydroxyl/carboxyl groups are mainly ascribed to decarboxylation

and dehydration of the starting materials [30,31]. The emerging aromatic clusters at 1690 cm^{-1} are a noticeably characteristic of hydrochars and result from dehydration reactions of reactive intermediates and followed polymerization [7,30]. The clusters are not represented in the spectra of pristine bakery waste as it only contains aliphatic compounds. In contrast, these observations cannot be made for HC-SCG, displayed in Fig. 3B. The C = O vibrations at 1750 cm^{-1} and the C–H stretch at 2774 – 2983 cm^{-1} assigned to

carbonyl and methyl groups of e.g. fatty acids and caffeine are also found to be in the pure SCG sample [32]. Besides, the sharp peak at 1580 cm^{-1} is related to C = C and C = N vibrations of pyridine derivatives [33]. This concludes the remaining of thermally stable compounds even after HTC treatment. However, an obvious decrease of the absorption bands assigned to C–O (833 – 1207 cm^{-1}) and O–H (3028 – 3615 cm^{-1}) bonds is also resulting from decarboxylation and dehydration reactions during HTC.

The absorption bands at 490 – 662 cm^{-1} appearing in iron-doped HCs is most likely assigned to Fe–O stretch of iron oxide nanoparticles [34]. This, as well, confirms the presence of iron oxides in the hydrochar product. However, no assignable peak can be detected for MnO$_2$.

IR-spectra of the ACs (Fig. 3C and D) appear to be very similar due to thermal cracking of various chemical bonds as hydroxyl- and oxygen functional groups (e.g. ester, ether, carboxyl groups) such as great release of volatiles. It has to be noted, that the disappearance of the caffeine and fatty acid absorption bands is related to the thermal decomposition of these compounds at higher temperatures and the bond-breaking leading to formation of smaller molecules. A minor fraction of oxygen functional groups between 1000 and 1300 cm^{-1} are still contained in the carbon network based on incomplete oxidation of the samples, mostly deriving from cyclic esters and hydroxyl groups of phenols [35,36]. The pronounced vibration band between 1580 and 1640 cm^{-1} is distinctive of an advanced aromatization of the carbon network. As no obvious differences in the spectra from the ACs can be detected, IR spectroscopy alone cannot give a clear indication of the influence of metal oxide species on the ACs.

The considerations of the ^{13}C NMR spectra of SCG and HC-SGC in Fig. 4 give a more detailed and complementary understanding of the chemical compositions. Especially the signals between 10 and 40 ppm require more attention in case of the HCs. Generally, the methyl groups of hemicellulose are located between 20 and 30 ppm [37]. Since HTC causes a degradation of the biopolymer, the signals decrease in the HC products due to elimination of these groups. Simultaneously, the resonance bands assigned to methyl groups of fatty acids and caffeine are present within the region of 10 – 40 ppm [38,39]. Thus, these signals become more visible as hemicellulose is decomposed (Fig. 4B and C). This indicates the superimposition of methyl resonance bands from hydrothermally stable compounds in case of pristine SCG (Fig. 4A). Note that the signals ascribed to alkyl groups of caffeine and fatty acids do not increase in absolute values, but only relatively to the decreasing resonance bands. The decreasing intensity of the signal at 50 – 95 ppm such as between 167 and 180 ppm are due to decarboxylation reactions, which was also already hinted in the IR-spectra. Note, that an additional signal between 180 and 185 ppm and a broad one at 210 ppm (only slightly above the baseline) can be observed. The latter is most likely due to decarboxylation reactions leading to a decrease in the broad signal between 167 and 180 ppm and the reformation to carbonyl groups (210 ppm) [37]. This was not observed in the IR spectra, due to low changes in intensity of the carbonyl group absorption bands. The crucial altering of the range between 60 and 95 ppm is not only assigned to the cracking of oxygen bonds (ester and ether groups) but also indicates the hydrolysis of cellulose and possible decarboxylation of the biopolymer [37,40]. Furthermore, the spectrum of HTC-treated SCG shows a significant increase in the signals ascribed to aromatic compounds, implying the formation of an aromatic carbon structure, most likely due to aromatization of intermediate cellulose derivatives and other degradation products.

Minor changes observed in MnO$_2$-doped hydrochars, shown in Fig. 4C, can certainly not be ascribed to the influence of nanoparticles on the ongoing reactions during HTC. Paramagnetic interactions of MnO$_2$ are seen as higher signal to noise in the NMR

spectroscopy. However, the most significant differences to the spectrum of HTC-SCG is the lower aromaticity and higher ester intensity at 185 ppm. Latter especially visibly increases in presence of MnO$_2$ nanoparticles (Fig. 4C). This behavior cannot be fully explained. However, it might be ascribed to the interaction between Mn^{4+}-ion and the unshared pairs of –C = O bonds of carboxyl groups leading to formation of a weak complex [41]. This could also clarify the lower aromaticity, as the nanoparticles hinder polymerization of furfural moieties and thus the structural formation of an aromatic carbon network.

4.3. Electrical conductivity

Yet, the enhancement and deterioration, respectively, of physical properties of the activated carbons emerges from electrical conductivity (EC) study (Fig. 5A and B). In general, the conductivity of carbonaceous materials depends on the arrangement of the carbon matrix on a molecular scale, such as carbon content and amount of sp^2-hybridized carbon atoms. Macroscopic impacts (e.g. bulk density and particle contact) also play a major role in this context. Carbon blacks differ by high carbon contents up to 99% and both, crystalline (ordered) and amorphous (disordered) fractions [42]. In contrast, activated carbons are porous materials consisting of disordered sections, lower carbon and correspondingly higher ash contents. Therefore, a collection of several carbon atoms with different hybridization states in activated carbons can be assumed. The compression of the carbon materials leads to an improved delocalization of πelectrons across all the adjacent aligned p orbitals. Although this facilitates charge carrier mobility due to enhanced contact between the particles, carbon black achieves superior conductivity values resulting from the foresaid characteristics. Regarding the bulk density, carbon black shows a higher compressibility at maximum bearing pressure. For instance, its bulk density at 1250 kPa is around 0,78 g/cm^3, while for pristine ACs only 0,15 – 0,32 g/cm^3 can be calculated. This especially relies on the pore network of the synthesized ACs and air trapped inside it, which is directly relatable to the lower conductivity [43].

Higher ECs of AC-SCG might be ascribed to the composition of the corresponding HCs and thermochemical reactions during activation. By thermal cracking of lipids, lignin and other organic compounds, which are still intact in the carbon matrix of the corresponding hydrochars, the formation of new atomic bonds and cross-linking of the carbon matrix can be proposed. From the previous observations provided by SEM images (Fig. 2B and C) the adsorption of MO-nanoparticles in case of HC-SCG has been assumed. Therefore, the following conclusions can be drawn about the higher electrical conductivity of the corresponding iron-doped ACs. An improved contact between the iron species and carbon particles could result in lower intrinsic resistance of the sample. This especially is considered when MO-species are superficially adherent to the AC and not incorporated in the pore network of the AC particles [16]. In fact, it is reasonable to assign the overall lower electrical conductivity of MO-doped AC-BW samples to the sheathing effects of the nanoparticles by carbon microspheres. A sluggish electron transfer by metal species entrapped inside the pores of the carbon and insufficient contact between the MO-nanoparticles and the carbon matrix can be assumed [21,16]. This might lead to higher intrinsic resistance of the MO-doped AC-BW samples compared to the undoped reference. The generally lower EC of MnO$_2$-doped ACs might be ascribed to the poor conductivity of amorphous MnO$_2$ or its reduction product, since unstructured metal oxides are known for their higher intrinsic resistivity [16]. MnO$_2$ particles also exhibited a much larger particle size compared to iron oxides in the hydrochars. Thus a small contact area between the particles is to be considered when compressing the samples,

compared to a finer distribution of smaller particles in case of Fe_2O_3- and Fe_3O_4-doped ACs.

4.4. Electrochemical properties

The different shapes of the CV curves shown in Fig. 6 are attributed to various factors occurring during electrochemical testing of the prepared electrodes. The higher obtained specific capacitance at lower scan rates is contributed by more charge carriers diffusing into the pore systems [44]. That results into a higher charge storage due to electrostatic interactions and specific adsorption across the electrical double layer and electrode–electrolyte-interface (EEI), respectively.

However, none of the investigated materials exhibit the rectangular CV-profile of an ideal supercapacitor. The high slope and oval shape of the curves is ascribed to the high intrinsic resistance of the ACs. As the potential feed decreases from 100 mV^*s^{-1} to 5 mV^*s^{-1}, a more irreversible behavior of the working electrode can be observed, as the cathodic peak is diminished or barely pronounced. This indicates sluggish electron transfers [45]. Regarding the electrolyte, a maximum ionic conductivity is reached at a concentration of 1 M H_2SO_4 in aqueous solution [46]. This might be restricting for obtaining a high specific capacitance in our case, since the electrolyte concentration used is only 0,5 M.

The electrolyte concentration is certainly not the determining factor concerning the poor electrochemical perfomance of the electrodes. It has been proven that the charge carrier distribution on the electrode surface and within the pores of the activated carbon particles has a major influence on the energy storage properties for electrochemical application [47]. The physical instability of the prepared electrodes as well as the inhomogeneity of the coating might result in inconsistent concentration gradients of adsorbed ions across the EEI, thus leading to formation of an unstable electical double layer. The sample properties discussed in chapter 4.3 also have to be considered, especially when nanoparticles are present within the pore system of the ACs. Several authors postulated a lower accessibility of the pore network due to clogging of cavities by metal species [16,43]. In this context, the electron exchange might be blocked by hindering the adsorption of charge carriers, which leads to a decrease of the specific capacitance.

Waste biomass derived ACs generally exhibit capacitance values between 30 and 380F^*g^{-1} [48,49]. Various studies have reported that electrodes made from coffee grounds range between 69 and 368F^*g^{-1} [13,48,49]. In our work, MnO_2-doped AC-SCG and pristine AC-SCG, which show the highest values, obtain an average specific capacitance of 49,2 and 39,2F^*g^{-1}, respectively. Although, these results are lower compared to the results mentioned in the literature, it has to be emphasized that the measurements of the respective electrodes show a very high deviation (Fig. 7). For instance, MnO_2-doped AC-SCG and pristine AC-SCG of the first batch exhibit a specific capacitance of 11F^*g^{-1} and 9F^*g^{-1} with an irreversible CV profile at an operating scan rate of 5 mV^*s^{-1}. The respective replications show the reversible behavior of an ideal capacitor at much higher capacitance values. Particularly, these electrodes achieved 87F^*g^{-1} and 69F^*g^{-1}, which resembles the electrochemical performance of electrodes investigated by other authors under similar conditions [50–53]. In contrast, the corresponding reference AC-BW-MnO_2, which has the overall lowest measured capacitance, shows only little adhesion of the active material to the CB@Al carrier film, implying that most of the active material becomes detached during the measurement. This is expressed by oscillating sections in the CV profile throughout the measurement (not shown here). In this case, most of the measured capacitance is due to interactions between the electrolyte and the CB coating of the carrier film. We therefore believe that due to the

defective electrode preparation the capacitance values shown here are lower, but may be higher under faultless conditions.

For comparison, electrodes from industrial ACs (I-AC) were manufactured and electrochemically characterized. Fig. 7 depicts that the SXRO derived electrode exhibits a high specific capacitance, especially during fast scans at 100 mV^*s^{-1}. This could be ascribed to a high proportion of macropores of the steam activated carbon and better ion accessibility of the pores at higher scan rates. In contrast, SAE achieves similar results as the majority of electrodes derived from SCG and BW. In fact, the capacitance of MnO_2-doped AC-SCG and pristine AC-SCG is almost as good or even better than the prepared electrodes from industrial ACs at a scan rate of 5 mV^*s^{-1}. However, the results must be viewed critically, since the methodological error also apply to the electrodes prepared from SXRO and SAE activated carbon.

None of the MO-doped ACs show faradaic currents or redox behavior. This indicates that the chemical activation may have altered the electrochemical redox activity of the metal species due to carbothermic reduction or H_2SO_4 might be unsuitable for our electrochemical setup. It can be proposed that the utilized metal species may not show the desired redox behavior towards the H_2SO_4 electrolyte. Many authors reported redox activities of MnO_2, Fe, Fe_2O_3 and Fe_3O_4 in basic electrolytes like KOH and NaOH [18,54–57]. However, we were not able to adapt these methods due to corrosion of the aluminum foil in basic solutions. Metal iron and iron oxides are also used as active materials for oxygen reduction reactions (ORR) [58,59]. In this case, the reaction takes place in both, acidic (e.g. H_2SO_4) or alkaline electrolytes, at 0,7 V and 1,23 V depending on a two- and four-electron oxygen reduction pathway, respectively [60]. This is undesirable for pseudocapacitors as these reactions occur irreversibly and may result in electrolyte degradation. Manganese species can also participate in reduction reactions with protons of dissociated sulfuric acid [61]. These reactions occur at higher potentials (~1,2 V) and result in dissolution of Mn^{2+}-ions [62]. As mentioned before, the high iron and manganese contents can also influence the energy storage mechanisms. This must be considered especially due to their large particle size, inhomogeneous distribution on the electrode surface and their presence within the pore structure of the AC. The accessibility of metal species for charge carriers is crucial for inducing faradic charge transfers. When located in the pore system, the redox active sites of the metal oxides may not be available for ions due to diffusion limitations [21].

4.5. Activated carbon as electrode materials for EDLC

Activated carbon is a promising material for EDLC electrodes, since it can be produced from sustainable raw materials using the conversion techniques applied here. A porous surface structure is essential for the energy storage mechanisms on the electrolyte–electrode-interface. A great benefit is the application of these porous carbons both as anode and cathode material for supercapacitors. Therefore, a variety of activated carbon can be fabricated, which differ only in their functionalization, e.g. N-, P- or metal oxide doping, with the intention to favor or facilitate ongoing redox reactions at the electrodes in supercapacitors and to achieve higher specific capacitance [4,31,63]. However, regarding only ACs, it has been proven that high carbon contents contribute to good electrochemical performance of the electrodes [43]. An HTC pretreatment with subsequent chemical activation of the starting materials seems to be the right approach to accomplish this. The insertion of MO-nanoparticles after thermochemical treatment is perhaps more favorable regarding the carbon yield, as more of the carbon content from the starting material remain in the product (table 1), and the accessibility of the pore network by diffusive ions from the electrolyte can be improved.

5. Conclusion

In this work, we demonstrated a facile technique of in situ doping of hydrochars with heterogeneous atoms carried out under hydrothermal conditions and a subsequent chemical activation process derived from biomass residues. Conversion and restructuring of the carbon matrix from BW lead to a higher incorporation of MO-nanoparticles as in case of solid-to-solid conversion of SCGs. It has been observed that Fe_2O_3 nanoparticles were reduced to Fe_3O_4 during HTC treatment.

Electrochemical analysis showed an overall higher capacitance for activated carbons of SCGs with a highest of $87F^*g^{-1}$ at a scan rate of $5\ mV^*s^{-1}$ for MnO_2-doped ACs. This also indicates a conversion product from HTC that undergoes solid-to-solid conversion, to be more suitable for electrochemical applications. The produced materials are comparable to industrial activated carbons with respect to the capacitance. Some materials, especially derived from SCG as starting material, largely exceed the capacitance of the industrial ones. Anyway, concerning the production of electrodes a significant improvement is necessary to improve the reproducibility. Despite this, conversion of agricultural waste and their use in energy storage systems, can be seen as a sustainable and effective approach for future energy solutions.

Declaration of Competing Interest

The authors declare that they have no known competing financial interests or personal relationships that could have appeared to influence the work reported in this paper.

Acknowledgements

References

[1] S. Iqbal, H. Khatoon, A. Hussain Pandit, S. Ahmad, Recent development of carbon based materials for energy storage devices, Mater. Sci. for Energy Technol. 2 (2019) 417–428.

[2] A.C. Forse, C. Merlet, J.M. Griffin, C.P. Grey, New Perspectives on the Charging Mechanisms of Supercapacitors, J. Am. Chem. Soc. 138 (18) (2016) 5731–5744.

[3] A. Eftekhari, The mechanism of ultrafast supercapacitors, J. Mater. Chem. A 6 (7) (2018) 2866–2876.

[4] L. Zhou, H. Cao, S. Zhu, L. Hou, C. Yuan, Hierarchical micro-/mesoporous N- and O-enriched carbon derived from disposable cashmere: a competitive cost-effective material for high-performance electrochemical capacitors, Green Chem. 17 (2015) 2373–2382.

[5] S. Ghosh, R. Santhosh, S. Jeniffer, V. Raghavan, G. Jacob, K. Nanaji, P. Kollu, S.K. Jeong, A.N. Grace, Natural biomass derived hard carbon and activated carbons as electrochemical supercapacitor electrodes, Sci. Rep. 1 (2019) 16315.

[6] H. Lu, X.S. Zhao, Biomass-derived carbon electrode materials for supercapacitors, Sustainable Energy Fuels 1 (6) (2017) 1265–1281.

[7] M. Sevilla, A. Fuertes, Chemical and Structural Properties of Carbonaceous Products Obtained by Hydrothermal Carbonization of Saccharides, Chem. Eur. J. 15 (16) (2009) 4195–4203.

[8] A. Funke, F. Ziegler, Hydrothermal carbonization of biomass: A summary and discussion of chemical mechanisms for process engineering, Biofuels, Bioprod. Bioref. 4 (2) (2010) 160–177.

[9] A. Jain, R. Balasubramanian, M.P. Srinivasan, Hydrothermal conversion of biomass waste to activated carbon with high porosity: A review, Chem. Eng. J. 238 (2016) 789–805.

[10] B.o. Hu, K. Wang, L. Wu, S.-H. Yu, M. Antonietti, M.-M. Titirici, Engineering Carbon Materials from the Hydrothermal Carbonization Process of Biomass, Adv. Mater. 22 (7) (2010) 813–828.

[11] X. Cui, M. Antonietti, S.-H. Yu, Structural Effects of Iron Oxide Nanoparticles and Iron Ions on the Hydrothermal Carbonization of Starch and Rice Carbohydrates, Small 2 (6) (2006) 756–759.

[12] K. Lotz, A. Wütscher, H. Düdder, C.M. Berger, C. Russo, K. Mukherjee, G. Schwaab, M. Havenith, M. Muhler, Tuning the Properties of Iron-Doped Porous Graphitic Carbon Synthesized by Hydrothermal Carbonization of Cellulose and Subsequent Pyrolysis, ACS Omega 4 (2) (2019) 4448–4460.

[13] T.E. Rufford, D. Hulicova-Jurcakova, Z. Zhu, G.Q. Lu, Nanoporous carbon electrode from waste coffee beans for high performance supercapacitors, Electrochem. Commun. 10 (10) (2008) 1594–1597.

[14] Ł. Kolanowski, M. Graś, M. Bartkowiak, B. Doczekalska, G. Lota, Electrochemical Capacitors Based on Electrodes Made of Lignocellulosic Waste Materials, Waste Biomass Valor 11 (7) (2020) 3863–3871.

[15] F. Shkal, S.G. Lopez, D. Slocombe, A. Porch, Microwave Characterization of Activated Carbons, JCC 06 (01) (2018) 112–123.

[16] A. Barroso-Bogeat, M. Alexandre-Franco, C. Fernández-González, A. Macías-García, V. Gómez-Serrano, Electrical conductivity of activated carbon–metal oxide nanocomposites under compression: a comparison study, Phys. Chem. Chem. Phys. 16 (45) (2014) 25161–25175.

[17] Y. Ren, Q. Xu, J. Zhang, H. Yang, B.o. Wang, D. Yang, J. Hu, Z. Liu, Functionalization of Biomass Carbonaceous Aerogels: Selective Preparation of MnO 2 @CA Composites for Supercapacitors, ACS Appl. Mater. Interfaces 6 (12) (2014) 9689–9697.

[18] L. Yu, G.Z. Chen, Redox electrode materials for supercapatteries, J. Power Sources 326 (2016) 604–612.

[19] T. Wang, Q. Le, X. Guo, M. Huang, X. Liu, F. Dong, J. Zhang, Y.X. Zhang, Preparation of Porous Graphene@Mn 3 O 4 and Its Application in the Oxygen Reduction Reaction and Supercapacitor, ACS Sustainable Chem. Eng. 7 (1) (2019) 831–837.

[20] S. Yan, K.P. Abhilash, L. Tang, M. Yang, Y. Ma, Q. Xia, Q. Guo, H. Xia, Research Advances of Amorphous Metal Oxides in Electrochemical Energy Storage and Conversion, Small 4 (2019) 1–30.

[21] V. Hoffmann, C. Rodriguez Correa, D. Sautter, E. Maringolo, A. Kruse, Study of the electrical conductivity of biobased carbonaceous powder materials under moderate pressure for the application as electrode materials in energy storage technologies, GCB Bioenergy 11 (1) (2019) 230–248.

[22] D. Jung, M. Zimmermann, A. Kruse, Hydrothermal Carbonization of Fructose: Growth Mechanism and Kinetic Model, ACS Sustain. Chem. Eng. 6 (11) (2018) 13877–13887.

[23] S.I. Mussatto, E.M.S. Machado, S. Martins, J.A. Teixeira, Production, Composition, and Application of Coffee and Its Industrial Residues, Food Bioprocess Technol 4 (5) (2011) 661–672.

[24] D. Kim, K. Lee, D. Bae, K.Y. Park, Characterizations of biochar from hydrothermal carbonization of exhausted coffee residue, J. Mater. Cycles Waste Manag. 19 (3) (2017) 1036–1043.

[25] C. Rodríguez Correa, M. Stollovsky, T. Hehr, Y. Rauscher, B. Rolli, A. Kruse, Influence of the Carbonization Process on Activated Carbon Properties from Lignin and Lignin-Rich Biomasses, ACS Sustain. Chem. Eng. 5 (9) (2017) 8222–8233.

[26] S. Zhang, L. Tao, Y. Zhang, Z. Wang, G. Gou, M. Jiang, C. Huang, Z. Zhou, The role and mechanism of K2CO3 and Fe3O4 in the preparation of magnetic peanut shell based activated carbon, Powder Technol. 295 (2016) 152–160.

[27] W.K. Jozwiak, E. Kaczmarek, T.P. Maniecki, W. Ignaczak, W. Maniukiewicz, Reduction behavior of iron oxides in hydrogen and carbon monoxide atmospheres, Appl. Catal. A: Gener. 326 (1) (2007) 17–27.

[28] J.F. Lu, C.J. Tsai, Reduction kinetics of hematite to magnetite under hydrothermal treatments, RSC Adv. 5 (22) (2015) 17236–17244.

[29] J.F. Lu, C.J. Tsai, Hydrothermal phase transformation of hematite to magnetite, Nanoscale Res. Lett. 9 (2014) 1–8.

[30] M. Sevilla, A.B. Fuertes, The production of carbon materials by hydrothermal carbonization of cellulose, Carbon 47 (9) (2009) 2281–2289.

[31] J.W. Straten, P. Schleker, M. Krasowska, E. Veroutis, J. Granwehr, A.A. Auer, W. Hetaba, S. Becker, R. Schlögl, S. Heumann, Nitrogen-Functionalized Hydrothermal Carbon Materials by Using Urotropine as the Nitrogen Precursor, Chem. Eur. J. 24 (47) (2018) 12298–12317.

[32] L.C.O. Silva, L.S. Oliveira, A.S. Franca, Fourier Transform Infra-Red (FTIR) spectroscopy applied to the detection of roasted coffee adulteration with spent coffee grounds, PACCON - Pure Appl. Chem. Int. Conf. (2011) 1-5.

[33] N. Reis, A.S. Franca, L.S. Oliveira, Performance of diffuse reflectance infrared Fourier transform spectroscopy and chemometrics for detection of multiple adulterants in roasted and ground coffee, Food Sci. Technol. 2 (2013) 395–401.

[34] S.W. Hwang, A. Umar, G.N. Dar, S.H. Kim, R.I. Badran, Synthesis and Characterization of Iron Oxide Nanoparticles for Phenyl Hydrazine Sensor Applications, sens lett 12 (1) (2014) 97–101.

[35] A. Allwar, Characteristics of Pore Structures and Surface Chemistry of Activated Carbons by Physisorption, Ftir And Boehm Methods, IOSR J. Appl. Chem. 1 (2012) 9–15.

[36] A.P. Terzyk, The influence of activated carbon surface chemical composition on the adsorption of acetaminophen (paracetamol) in vitro, Colloids Surf. A: Physicochem. Eng. Asp. 177 (1) (2001) 23–45.

[37] L. Calucci, D.P. Rasse, C. Forte, Solid-State Nuclear Magnetic Resonance Characterization of Chars Obtained from Hydrothermal Carbonization of Corncob and Miscanthus, Energy Fuels 27 (1) (2013) 303–309.

[38] T.I. Hämäläinen, S. Sundberg, M. Mäkinen, S. Kaltia, T. Hase, A. Hopia, Hydroperoxide formation during autoxidation of conjugated linoleic acid methyl ester, Eur. J. Lipid Sci. Technol. 103 (9) (2001) 588–593.

[39] E. Kolehmainen, Caffeine as a Gelator, Gels 1 (2016) 1–10.

[40] F. Wei, K. Furihata, M. Koda, F. Hu, R. Kato, T. Miyakawa, M. Tanokura, 13 C NMR-Based Metabolomics for the Classification of Green Coffee Beans According to Variety and Origin, J. Agric. Food Chem. 60 (40) (2012) 10118–10125.

[41] M. Bicker, S. Endres, L. Ott, H. Vogel, Catalytical conversion of carbohydrates in subcritical water: A new chemical process for lactic acid production, J. Mol. Catal. A-Chem. 1–2 (2005) 151–157.

[42] D. Pantea, H. Darmstadt, S. Kaliaguine, C. Roy, Electrical conductivity of conductive carbon blacks: influence of surface chemistry and topology, Appl. Surf. Sci. 1–4 (2003) 181–193.

[43] V. Hoffmann, D. Jung, J. Zimmermann, C. Rodriguez Correa, A. Elleuch, K. Halouani, A. Kruse, Conductive Carbon Materials from the Hydrothermal Carbonization of Vineyard Residues for the Application in Electrochemical Double-Layer Capacitors (EDLCs) and Direct Carbon Fuel Cells (DCFCs), Materials 10 (2019) 1–33.

[44] G.A.M. Ali, L.L. Tan, R. Jose, M.M. Yusoff, K.F. Chong, Electrochemical performance studies of MnO 2 nanoflowers recovered from spent battery, Mater. Res. Bull. 60 (2014) 5–9.

[45] H. Hammani, W. Boumya, F. Laghrib, A. Farahi, S. Lahrich, A. Aboulkas, M.A. El Mhammedi, Electrocatalytic effect of NiO supported onto activated carbon in oxidizing phenol at graphite electrode: Application in tap water and olive oil samples, J. Assoc. Arab Univ. Basic Appl. Sci. 1 (2017) 26–33.

[46] C. Zhong, Y. Deng, W. Hu, J. Qiao, L. Zhang, J. Zhang, A review of electrolyte materials and compositions for electrochemical supercapacitors, Chem. Soc. Rev. 44 (21) (2015) 7484–7539.

[47] J. Kowal, E. Avaroglu, F. Chamekh, A. Šenfelds, T. Thien, D. Wijaya, D.U. Sauer, Detailed analysis of the self-discharge of supercapacitors, J. Power Sources 196 (1) (2011) 573–579.

[48] W. Gu, G. Yushin, Review of nanostructured carbon materials for electrochemical capacitor applications: advantages and limitations of activated carbon, carbide-derived carbon, zeolite-templated carbon, carbon aerogels, carbon nanotubes, onion-like carbon, and graphene, WIREs Energy Environ. 5 (2014) 424–473.

[49] A.M. Abioye, F.N. Ani, Recent development in the production of activated carbon electrodes from agricultural waste biomass for supercapacitors: A review, Renew. Sustain. Energy Rev. 52 (2015) 1282–1293.

[50] J. Choi, C. Zequine, S. Bhoyate, W. Lin, X. Li, P. Kahol, R. Gupta, Waste Coffee Management: Deriving High-Performance Supercapacitors using Nitrogen-Doped Coffee-Derived Carbon, J. Carbon Res. 3 (2019) 44.

[51] M. Zakir H. Kasim I. Raya Y. Lamba A.B. Nuratisah Jorge, Performance of Candlenut Shell (Alleuretus moluccana) Based Supercapacitor Electrode with Acid Electrolytes and Their Salts IOP Conf. Ser.: Mater. Sci. Eng. 619 2019 12042

[52] J.M.V. Nabais, J.G. Teixeira, I. Almeida, Development of easy made low cost bindless monolithic electrodes from biomass with controlled properties to be used as electrochemical capacitors, Bioresour. Technol. 3 (2011) 2781–2787.

[53] K. Wasiński, P. Nowicki, P. Półrolniczak, M. Walkowiak, R. Pietrzak, Processing Organic Waste Towards High Performance Carbon Electrodes for Electrochemical Capacitors, Int. J. Electrochem. Sci. 12 (2017) 128–143.

[54] X. Du, C. Wang, M. Chen, Y. Jiao, J. Wang, Electrochemical Performances of Nanoparticle Fe3O4/Activated Carbon Supercapacitor Using KOH Electrolyte Solution, J. Phys. Chem. 6 (2009) 2643–2646.

[55] Y. Li, L. Kang, G. Bai, P. Li, J. Deng, X. Liu, Y. Yang, F. Gao, W. Liang, Solvothermal Synthesis of Fe2O3 Loaded Activated Carbon as Electrode Materials for High-performance Electrochemical Capacitors, Electrochim. Acta (2014) 67–75.

[56] P. Krawczyk, T. Rozmanowski, Preparation and electrochemical properties of EG/Fe2O3/C composite, Ionics 21 (1) (2015) 59–66.

[57] W. Feng, M. Liu, J. Liu, Y. Song, F. Wang, Well-defined Fe, Fe 3 C, and Fe 2 O 3 heterostructures on carbon black: a synergistic catalyst for oxygen reduction reaction, Catal. Sci. Technol. 19 (2018) 4900–4906.

[58] C. Goswami, K.K. Hazarika, P. Bharali, Transition metal oxide nanocatalysts for oxygen reduction reaction, Mater. Sci. Technol. 2 (2018) 117–128.

[59] H. Xiao, Z.-G. Shao, G. Zhang, Y. Gao, W. Lu, B. Yi, Fe–N–carbon black for the oxygen reduction reaction in sulfuric acid, Carbon 57 (2013) 443–451.

[60] A. Kulkarni, S. Siahrostami, A. Patel, J.K. Nørskov, Understanding Catalytic Activity Trends in the Oxygen Reduction Reaction, Chem. Rev. 5 (2018) 2302–2312.

[61] Y.U. Jeong, A. Manthiram, Nanocrystalline Manganese Oxides for Electrochemical capacitors, J. Electrochem. Soc. 11 (2002) A1419–A1422.

[62] M.S. Bafghi, A. Zakeri, Z. Ghasemi, M. Adeli, Reductive dissolution of manganese ore in sulfuric acid in the presence of iron metal, Hydrometallurgy 2-4 (2008) 207–212.

[63] Y. Liu, J. Ruan, S. Sang, Z. Zhou, Q. Wu, Iron and nitrogen co-doped carbon derived from soybeans as efficient electro-catalysts for the oxygen reduction reaction, Electrochim. Acta 215 (2016) 388–397.